

First-principles investigation of CZTS Raman spectra

S. P. Ramkumar^{1,2,3,*}, G. Petretto^{1,3}, W. Chen^{1,3}, H. P. C. Miranda^{1,3,4}, X. Gonze^{1,3,5} and G.-M. Rignanese^{1,3}¹IMCN-MODL, Université catholique de Louvain, Chemin des Étoiles, 8, B-1348 Louvain-la-Neuve, Belgium²Department of Materials Science and Engineering, University of California, Merced, California 95343, USA³European Theoretical Spectroscopy Facility (ETSF)⁴VASP Software GmbH, Sensengasse 8/16, 1090 Vienna, Austria⁵Skolkovo Institute of Science and Technology, Skolkovo Innovation Center Nobel St. 3, Moscow, 143026, Russia

(Received 12 January 2021; revised 13 January 2022; accepted 4 March 2022; published 22 March 2022)

Cu₂ZnSnS₄ (CZTS) is an earth-abundant photovoltaic absorber material predicted to provide a sustainable solution for commercial solar applications. However, the efficiency of such solar cells is rather limited, cation disorder being often designated as the culprit. Raman spectroscopy has been widely used to characterize CZTS. Nonetheless, the interpretation of the spectra in terms of the atomic-scale disorder is precluded by the lack of consensus between theoretical and experimental results. In particular, there is a strong discrepancy in the relative intensities of the two prominent *A* phonon peaks of the spectra. In the present study, we demonstrate that the internal parameters characterizing the position of the S atoms strongly influence these intensities. We show that agreement with experiments can be completely recovered when adopting the geometry computed using a hybrid exchange-correlation functional. Finally, using special quasirandom structures, we demonstrate that the disorder only leads to a change of the shape of the Raman peaks (tailing or leading edges, shouldering and splitting). This could be exploited to assess the quality of the sample in terms of how ordered they are.

DOI: [10.1103/PhysRevMaterials.6.035403](https://doi.org/10.1103/PhysRevMaterials.6.035403)

I. INTRODUCTION

In light of climate change due to greenhouse gas emissions, photovoltaics (PV) is expected to play an important role to meet the growing energy demand on a sustainable basis [1]. Si solar cells currently dominate the PV market, but the more versatile thin-film technology [mainly, based on CdTe and CuIn_xGa_{1-x}(S, Se)₂] has almost matched the former in performance, reaching efficiencies close to 21% [2]. Nonetheless, almost all of the present commercially available PV technologies suffer from various drawbacks (be it the amount of energy needed to fabricate them, the low availability or the toxicity of one or more constituting elements), which will likely limit their role in large-scale applications. To counter such drawbacks, PV devices based on Cu₂ZnSnS₄ (CZTS) with earth abundant and nontoxic elements have garnered tremendous interest in the last decade. As a downside, their record efficiency is only about 11% [3], making them commercially not viable at the moment. One major reason for the low efficiency in CZTS has been attributed to the presence of Cu-Zn disorder [4,5].

The nature of the Cu-Zn disorder has been the subject of many experimental and theoretical studies, including x-ray and neutron diffraction [6], Raman spectra [7–10], nuclear magnetic resonance (NMR) [11,12], and photoluminescence measurements [13]. Experimentally, CZTS is found to crystallize in the kesterite (KS) structure (with space group *I*4̄) [6,14,15], illustrated in Fig. 1(a). It has alternating Cu/Zn

and Cu/Sn planes along the [001] direction and four different cationic sites: One Cu is located at the Wyckoff position *2a* (0,0,0), the other Cu at *2c* (0,1/2, 1/4), Zn at *2d* (0,1/2, 3/4), and Sn at *2b* (0,0,1/2). Until recently, the generally accepted picture was that, above the critical temperature *T_c* (ranging between 533 and 552 K [7,16]), KS evolves to CZ-PD, which is characterized by a disorder in the Cu-Zn planes with the *2c* and *2d* sites occupied on average by 1/2 Cu and 1/2 Zn [Fig. 1(b)]. However, a high-resolution neutron diffraction experiment [17], soon followed by theoretical works relying on density functional theory (DFT) [18–20], showed that KS actually goes to CZ-FD, a phase in which all Cu-Zn sites are fully disordered, with the *2a*, *2c*, and *2d* sites occupied on average by 2/3 Cu and 1/3 Zn [Fig. 1(c)].

While a good agreement has been reached between the theoretical and experimental observations in terms of phase characteristics and partial occupancy, this is not completely the case for the vibrational properties and, in particular, for Raman spectroscopy which has been widely used to try to characterize CZTS [10,12,21–24]. Experimental Raman spectra [10,12,21–24] typically show two prominent peaks at 287 and 331 cm⁻¹ with the second one displaying a higher intensity (see Fig. 2).

From the theoretical standpoint, all previous theoretical works [8–10,24,26,27] have focused on ordered structures. Most of them relied on semilocal exchange-correlation (XC) functionals such as local density approximation (LDA) or generalized gradient approximation (GGA). In this framework, none of the investigated phases was found to present a spectrum corresponding to the experimental one within the error bar that is usually expected. Typically, the higher frequency phonon modes, which are predominantly dominated by the

*Present address: Micron Tech. Operations India LLP, Rd number 1, Financial district, Nanakramguda, Telangana 500032, India.

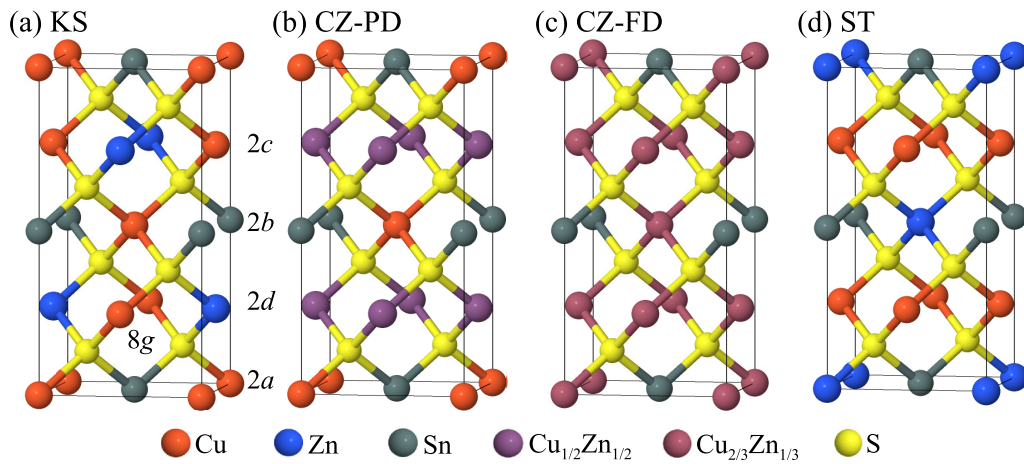


FIG. 1. Tetragonal unit cells of CZTS: (a) kesterite (KS), (b) Cu-Zn plane disordered (CZ-PD), (c) Cu-Zn fully disordered (CZ-FD), and (d) stannite (ST).

motion of S atoms, show a red shift of 15 cm^{-1} with respect to experiment. Furthermore, in the two earlier papers [8,9] in which the Raman intensities were calculated, the first prominent peak was found to be higher in intensity than the second one, in clear contrast with experimental findings.

Recently, Monserrat *et al.* [27] resolved one of these discrepancies, improving the agreement in terms of the phonon frequencies by using a hybrid XC functional which better accounts for the polarizabilities of the S atoms. However, they did not compute the Raman intensities and focused only on the phonon density of states. So the question is still open as to whether the remaining intensity discrepancy is to be ascribed

to the XC functional or to the presence of disorder in the structure.

In order to address this issue, we perform first-principles calculations based on density functional theory (DFT) [28] and density functional perturbation theory (DFPT) [29–31] investigating the effect of the XC functional on the internal geometry and connecting this to phonon frequencies and Raman intensities. We show that, when properly taken into account, these ingredients are sufficient to reconcile the experimental and theoretical picture of the vibrational properties. From the computation of the Raman spectra for simplified models of the disordered structures, we propose that the disorder is only responsible for a widening of the peaks without affecting significantly the intensities.

The paper is organized as follows. Section II describes the computational methods and the different structures considered in the study. In Sec. III, our main results are presented and discussed. We first focus on the ordered structures (Sec. III A) and present their structural (Sec. III A 1) and vibrational (Sec. III A 2) properties. In particular, the effect of exchange-correlation functionals (semilocal vs hybrid) is discussed. Section III A 3 provides an analysis of the calculated Raman spectra as function of the internal parameters. Finally, Sec. III B focuses on the effect of the disorder on the Raman spectra. Our conclusions are presented in Sec. IV.

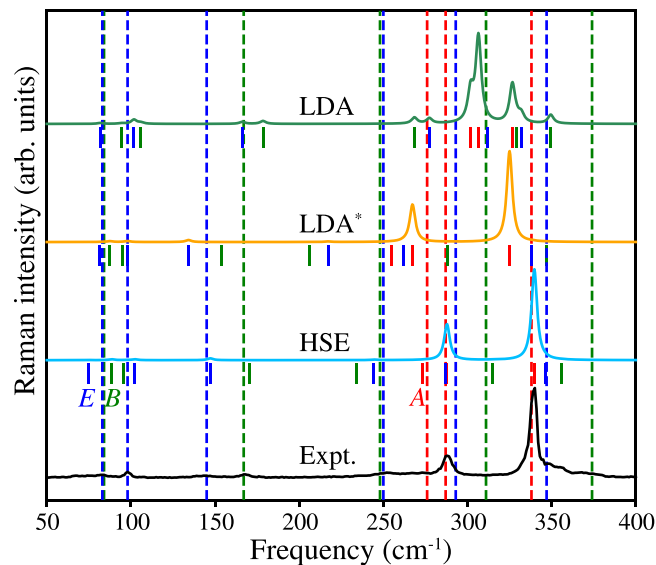


FIG. 2. Raman spectra of polycrystalline CZTS. The top three curves show the Raman spectrum for the KS structure, computed using LDA at the LDA relaxed geometry, LDA at the HSE relaxed geometry (LDA*), and HSE (using LDA* intensities), respectively. For comparison with experiments [21] (black curve at the bottom), a temperature of 300 K is chosen for the Bose-Einstein occupation factors. The red, green, and blue dotted lines denote the TO frequencies of A, B, and E modes obtained from polarized Raman measurements of Guc *et al.* [25].

II. COMPUTATIONAL DETAILS

The dynamical properties as well as Raman spectra are calculated with the ABINIT software package [32–34]. Norm-conserving (NC) pseudopotentials are used with $\text{Cu}(3s^23p^63d^{10}4s^1)$, $\text{Zn}(3s^23p^63d^{10}4s^2)$, $\text{Sn}(4d^{10}5s^25p^2)$, and $\text{S}(3s^23p^4)$ levels treated as valence states. These pseudopotentials have been generated using the ONCVSP package [35] and validated within the PSEUDODOJO framework [36,37].

Most of the calculations are performed on KS structures using the local density approximation (LDA) [38] for evaluating the XC energy. The wave functions for the density functional calculations are expanded using a plane-wave basis set up to a kinetic energy cutoff of 50 Ha. The Brillouin zone is sampled using a $6 \times 6 \times 6$ Monkhorst-Pack k -point grid [39].

The structures are fully relaxed with a tolerance of 1×10^{-5} Ha/Bohr (≈ 0.5 meV/Å) on the remaining forces.

The phonon frequencies are computed at the Γ point of the Brillouin zone. The Raman scattering efficiency of the phonon of frequency ω_m for a photon of frequency ω_i is defined as presented in Veithen *et al.* [40]:

$$I = (\omega_i - \omega_m)^4 |\mathbf{e}_o \cdot \boldsymbol{\alpha}_m \cdot \mathbf{e}_i|^2 \frac{n_m + 1}{2\omega_m}, \quad (1)$$

with \mathbf{e}_i and \mathbf{e}_o the incoming and outgoing light polarizations, n_m the temperature-dependent phonon occupation factor:

$$n_m = \frac{1}{e^{\omega_m/kT} - 1}. \quad (2)$$

The Raman susceptibility tensor $\boldsymbol{\alpha}^m$ for mode m is calculated as [40]

$$\alpha_{ij}^m = \sqrt{\Omega} \sum_{\kappa\beta} \frac{\partial \chi_{ij}^{(1)}}{\partial \tau_{\kappa\beta}} u_m(\kappa\beta), \quad (3)$$

where $\tau_{\kappa\beta}$ is the displacement of atoms in the sublattice κ along the β axis and u_m are the eigendisplacements. The susceptibility is approximated by its static value rather than being evaluated at the frequency of the incoming light and without taking into account the excitonic effects [41], which would be too computationally demanding. We take into account the polycrystalline nature of the experimental sample, i. e., considering intensities both in the parallel and perpendicular laser polarizations, and providing an average over all the possible orientations of the crystal as prescribed by Caracas and Banigan [42].

Hybrid functional calculations based on the HSE XC functional [43–45] were performed with the VASP [46] code using the projector augmented wave (PAW) [47] method. The structures were optimized with a convergence criterion on the total energy of 10^{-8} meV/atom and 1 meV/Å on the forces. While for KS and ST both atomic positions and lattice vectors were fully optimized, in the case of the CZ-PD and CZ-FD only the internal degrees of freedom were allowed to relax. In addition, for KS and ST we computed the phonon frequencies at the Γ point via finite displacements (or finite differences) as implemented in the PHONOPY package [48]. We considered a kinetic energy cut-off of 450 eV for truncating the plane-wave basis set. For sampling the Brillouin zone, we used Monkhorst-Pack k -point grids [39] centered at Γ : $4 \times 4 \times 4$ for KS and ST, $4 \times 4 \times 3$ for CZ-PD, and $3 \times 3 \times 4$ for CZ-FD.

As will be explained in the following sections, the structural parameters play a key role in determining the vibrational properties and thus phonon frequencies and Raman spectra have also been calculated using the LDA XC functional but adopting the HSE structure. These results will be referred to as LDA* in the following.

Based on the results from a previous study by some of us [9], we assume that the XC functional has a negligible effect on the Raman intensities. The HSE Raman spectra was thus calculated from Eq. (1) with the Raman susceptibilities obtained from LDA* [i.e., computed with ABINIT from LDA and NC pseudopotentials using Eq. (3)] and the phonon frequencies from HSE calculations with VASP.

TABLE I. Lattice constants and internal parameters KS and ST phases computed with LDA and HSE. The experimental data are taken from Ref. [52].

		a_0 (Å)	c_0 (Å)	u_x	u_y	u_z
KS	Expt.	5.427	10.871	0.756	0.757	0.872
	LDA	5.316	10.636	0.761	0.770	0.870
	HSE	5.448	10.857	0.755	0.758	0.872
ST	Expt.	5.449	10.757	0.757	$=u_x$	0.870
	LDA	5.316	10.637	0.760	$=u_x$	0.864
	HSE	5.418	10.916	0.755	$=u_x$	0.870

In order to understand the effect of disorder we also calculated Raman intensities for the CZ-PD, CZ-FD, and stannite (ST) phases. Special quasirandom structures (SQSs) with 16 and 24 atoms in the unit cells were used to represent the CZ-PD and CZ-FD phases, respectively [49]. The SQSs were generated by taking into account pair clusters up to the 6 nearest neighbors (NNs) and triplets up to the second NNs. Details on the geometry and correlation functions of the SQSs are described in Appendix A.

III. RESULTS AND DISCUSSION

A. Ordered structures

1. Structural properties

It has been observed that one of the shortcomings of standard DFT XC functionals is the difficulty of accurately reproducing the anion-cation bond lengths. This concretizes in the inaccuracy of the internal parameters and contributes to the errors in the prediction of the electronic band gap [50,51].

The KS phase displays space group $I\bar{4}$ ($N^\circ 82$), while the ST phase is in the space group $I\bar{4}2m$ ($N^\circ 121$), with more symmetries than that of KS, due to the introduction of mirror planes (same occupation of $2c$ and $2d$ sites) [15]. Both phases are tetragonal with only two lattice constants a_0 and c_0 . In both cases, the only internal degrees of freedom correspond to the position of the S atoms in the $8g$ and $8i$ Wyckoff sites, respectively. There are thus three internal parameters (u_x, u_y, u_z) with $u_x = u_y$ in ST.

The experimental values of the lattice constants and the internal parameters u along with those obtained from DFT calculations are reported in Table I. As expected, the HSE geometry is in much better agreement with experiments than the LDA one in terms of both the lattice constants and, especially, the internal parameters u . Notably, the values of u_x and u_y in KS are very close in HSE, as measured in the experiments, at variance with the results from LDA.

2. Vibrational properties

The phonon frequencies at the Γ point of the Brillouin zone have been computed using different approximations. In particular, phonon calculations have been carried out using the LDA and HSE XC functionals for the corresponding relaxed geometries.

Group theory analysis representing the acoustic and optic phonon modes at the Γ point of Brillouin zone provides the following irreducible representations. For KS structures (in

TABLE II. Calculated Γ -point phonon frequencies (in cm^{-1}) for the KS phase of CZTS for LDA, LDA*, and HSE. For the first two, both TO and LO frequencies were obtained, while for the last, only TO frequencies were computed. The experimental Raman (from Refs. [21], [22], and [25]) and IR (from Ref. [53]) frequencies are also shown for comparison.

Mode	Theory			Experiment			
	LDA	LDA*	HSE	Ref. [21]	Ref. [22]	Ref. [25]	Ref. [53]
A(1)	301.8	255.1	273.2	287	287	276	
A(2)	306.5	267.3	287.8	302		287	
A(3)	326.7	325.0	339.7	338	337	338	
B(TO1)	94.3	87.5	88.4	82	83	84	86
B(LO1)	95.4	88.1	89.0				
B(TO2)	105.9	95.1	95.5	97	97		
B(LO2)	106.1	95.1	95.6				
B(TO3)	178.5	154.1	170.4	164	166	167	168
B(LO3)	178.6	154.2	170.6				
B(TO4)	268.4	206.0	233.9	255	252	248	
B(LO4)	284.6	210.0	237.8	263		255	
B(TO5)	329.2	287.8	314.7	331		311	316
B(LO5)	333.0	288.6	315.4			320	
B(TO6)	349.5	347.0	355.7	353	353	352	
B(LO6)	359.0	348.7	357.2	374		374	
E(TO1)	81.8	81.6	74.5	68	66	83	68
E(LO1)	81.8	81.7	74.7				
E(TO2)	101.8	98.0	102.1	97	97	98	
E(LO2)	101.8	98.4	102.5				
E(TO3)	166.1	134.1	147.1	140	143	145	143
E(LO3)	166.2	134.5	147.4	151			
E(TO4)	277.3	217.1	244.4			250	255
E(LO4)	288.3	220.9	248.3	271	272	264	
E(TO5)	312.0	262.0	286.8	316		293	293
E(LO5)	314.4	264.8	289.5			300	
E(TO6)	331.9	337.9	346.2	347	347	347	351
E(LO6)	342.0	341.8	349.6	366		366	

the $I\bar{4}$ space group), we have

$$\Gamma = \underbrace{1B \oplus 1E}_{\text{Acoustic}} \oplus 3A \oplus \underbrace{6B \oplus 6E}_{\substack{\text{IR} \\ \text{Raman}}}$$

and for the remaining structures (in the $I\bar{4}2m$ space group) it is

$$\Gamma = \underbrace{1B_2 \oplus 1E}_{\text{Acoustic}} \oplus 2A_1 \oplus 2B_1 \oplus \underbrace{4B_2 \oplus 6E}_{\text{IR}} \oplus \underbrace{A_2}_{\text{Silent}}.$$

Based on the above, we can identify the Raman active phonon modes for the structures under consideration. In Table II, the computed LDA, LDA*, and HSE phonon frequencies for the KS structure are compared with experimental observations to provide a clear understanding on this aspect. For the KS structure, the mean absolute difference (MAD) between TO modes of LDA (resp. HSE) with respect to experiment [25] is 14.8 cm^{-1} (resp. 4.4 cm^{-1}). Further, the largest MAD for LDA are from the A modes with 18.9 cm^{-1} , while with HSE the A mode MAD is about 10 times smaller with a value of 1.8 cm^{-1} . This clearly shows the improved prediction of A modes frequencies from HSE, in agreement with the findings of Ref. [27]. While LDA* frequencies lead to MAD

values that are comparable with those of full LDA calculations (16.1 cm^{-1} for all the frequencies and 17.8 cm^{-1} for the A modes), they display a splitting of the A modes that is in very good agreement with the experimental frequencies.

It should be noted that the labels A(1), A(2), and A(3) used to identify the three A modes only refer to their order based on the phonon frequencies. As will be discussed below, these modes can undergo strong mixing under different approximations and we do not aim to define a label based on the mode features.

Figure 2 shows the calculated Raman spectra in comparison to the experimental spectrum of Dimitrievska *et al.* [21]. It should be reminded that the HSE spectrum combines the HSE phonon frequencies with the Raman susceptibilities coming from the LDA* calculation.

For frequencies below 150 cm^{-1} , all the theoretical spectra are similar to the experimental ones. But above that value, the experimental spectra are best represented by HSE. Therefore, we confirm the difference between LDA and HSE frequencies due to the peak shifts already observed in Ref. [27]. Furthermore, the use of the Raman intensities from the HSE structure also leads to an excellent agreement of the relative heights of the peaks: a silent A(1) and the intensity of A(2) smaller than the one of A(3). In fact, the LDA* spectrum decently reproduces the experimental one, aside from an overall shift of

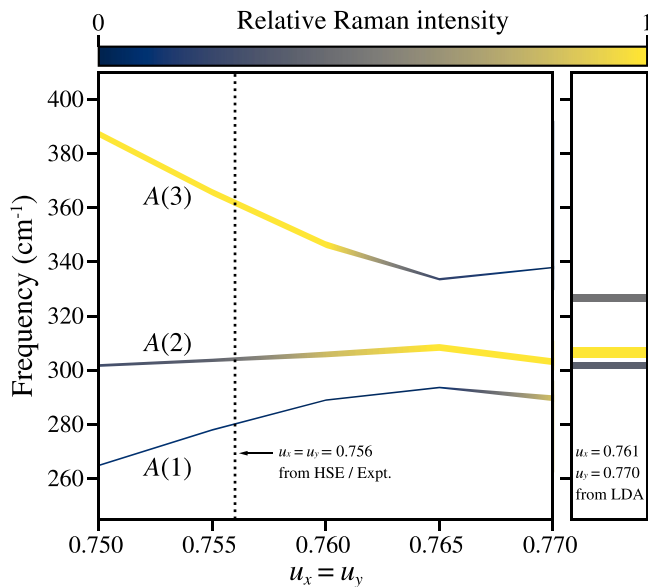


FIG. 3. The left panel shows the variation of the frequencies for the A phonon modes of KS structure calculated within the LDA approximation as a function of the u_x parameter. The evolution of the corresponding relative Raman intensities is indicated by the color and thickness of the lines. The calculations assume that $u_x = u_y$, which is almost true within HSE and experimentally. The approximated HSE and experimental value of u_x is indicated by the vertical dotted line. u_z is fixed at 0.870. The right panel reports the calculated values for the LDA geometry ($u_x \neq u_y$) for comparison.

the A peaks, while the LDA results provide incorrect relative intensities.

3. Influence of the internal parameters

We now turn to the difference between the peak intensities in LDA and LDA*. Inspired by the previously demonstrated dependence of the electronic band gap on the internal parameters u [50], we investigate the effect of the value of u on the vibrational properties and, in particular, on the A modes.

The first point to be noted is that, as shown in Appendix B, the whole contribution to the A modes comes from the displacements of the S atoms. In addition, the contribution to the displacements gets mixed when considering the different structures in the LDA approximation as opposed to the LDA* (see Fig. 7). Since the position of the S atoms and the distance from their neighbors is entirely controlled by the internal parameters u , it is expected that this value has a strong influence on their vibrational properties.

Figure 3 shows the dependence of the phonon frequencies and Raman intensities of the A modes on the value of the $u_x = u_y$ parameters for the KS phase. For simplicity, we chose to keep u_x equivalent to u_y given that this is approximately respected experimentally and when using HSE. Further discussion and plots on the dependence on u_y and u_z can be found in Appendix C.

While a change in the lattice parameters a and c leads to a simple and uniform rescaling of the phonon frequencies [9], it is clear from Fig. 3 that this is not the case when varying the internal parameters u . In particular, the $A(2)$ mode

remains quite stable in the considered u_x interval whereas $A(1)$ and $A(3)$ follow opposite trends: the former increases and the latter strongly decreases as a function of u_x , reaching an extremal point at $u_x = 0.765$. It is thus clear why the three A peaks are all packed in the same region of the spectra when employing the full LDA approximation. Similar trends can be observed for the dependence on u_y and u_z , with the $A(3)$ mode undergoing the largest variation (see Figs. 11 and 12). This is due to the fact that the nature of this mode strongly changes from purely parallel to the c axis to a mixed one, as shown in Fig. 7.

Similarly, the change of u induces a modification of the relative intensities of the A peaks that does not take place when just changing the lattice parameters. The $A(3)$ mode goes from being the peak with the strongest intensity in the range $0.750 < u_x < 0.760$ to be almost silent at the largest considered value. In turn, $A(1)$ and especially $A(2)$ increase their intensity, with the latter becoming the most intense peak for u_x above 0.760. At variance with the case of the phonon frequencies, trends are different when considering separately the change of u_y and u_z . In these cases the $A(3)$ mode keeps the highest intensity over all the explored ranges.

Such a variety in the behavior of the vibrational properties on the internal parameters demonstrates that it is indeed crucial to identify with high accuracy the position of the anion to also correctly reproduce the experimental vibrational properties. The excellent agreement of the HSE Raman spectra with the experimental one in Fig. 2 is thus a consequence of the ability of the HSE approximation of properly determining the correct geometry of the system.

We now discuss the role of the eigendisplacements in determining the Raman spectra for the different structures. Since the A phonon modes are entirely due to the displacements of the S atoms (see Fig. 7 of the Appendix B), we can focus on the motion of those atoms and describe them with respect to the tetrahedra that they form with the first-nearest-neighbor cations sitting on the $2a$, $2c$, and $2d$ sites present at the center of tetrahedra. More specifically, they can be expressed exactly as a linear combination of three ideal A modes (labeled \tilde{A}' , \tilde{A}'' , and \tilde{A}''') as schematically presented in Fig. 4. Such a decomposition is also particularly interesting for studying the Raman intensities using a bond polarizability model [54] where simple considerations can be made (see Appendix D).

Based on Eq. (3), we can relate the Raman susceptibility tensors for two different calculations using the transformation:

$$\tilde{\alpha}_{ij}^m = \sum_n M_{mn} \alpha_{ij}^n, \quad (4)$$

where \mathbf{M} is the matrix of the change of base in $\mathbb{R}^{3N_{\text{at}}}$ defined by the two sets of eigendisplacements. In particular, we can extract the Raman susceptibilities of the ideal modes \tilde{A} as an average of the values obtained from Eq. (4) over different values of u_x .

It is then possible to perform the inverse operation and compare the actual Raman spectra with the one calculated from the transformed susceptibilities. The spectra, limited to the A modes, for different values of $u_x = u_y$ are shown in Fig. 5. The excellent agreement between the two sets of spectra demonstrates how the main contribution in the change

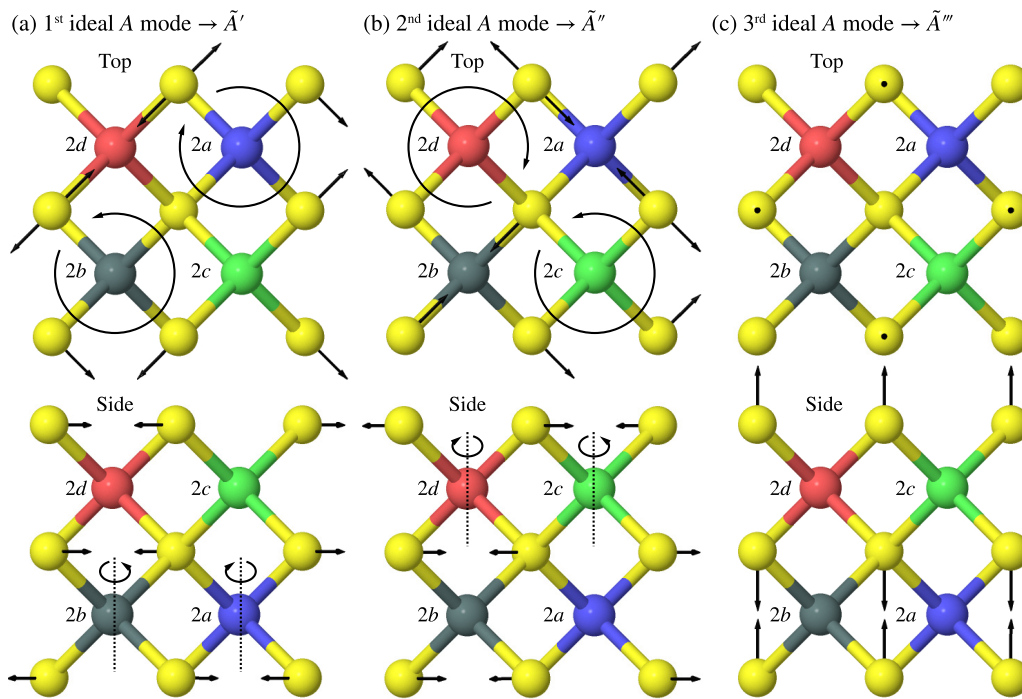


FIG. 4. Top and side views of the motion of the S atoms for the three ideal A modes (\tilde{A}' , \tilde{A}'' , and \tilde{A}'''). The circular arcs with arrows indicate a rigid rotation of a tetrahedron around an vertical axis reported as a dashed line in the side view. The Sn and S atoms are in grey and yellow respectively, while the atoms at the 2a, 2c, and 2d sites are in blue, green, and red. Their occupations are indicated in Fig. 1.

of the relative intensities of the peaks comes from the change in the eigendisplacements associated to the A modes as a function of the position of the sulfur atoms.

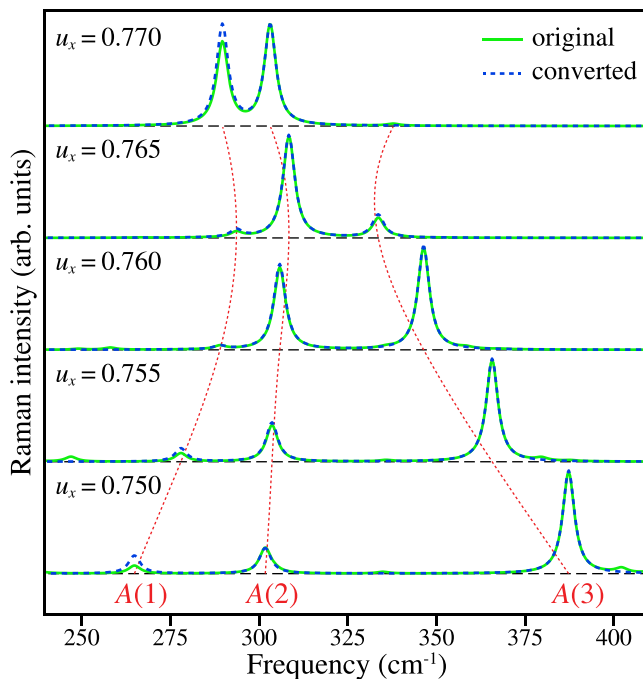


FIG. 5. Comparison between Raman spectra of the A modes computed within LDA (original) with those obtained from the transformation of the susceptibilities of the ideal modes \tilde{A} (converted) based on Eq. (4) as a function of $u_x = u_y = u_z$ fixed at 0.870.

Finally, these results provide further insights and a justification for using the LDA computed Raman intensities together with the HSE phonon frequencies in Fig. 2. In fact, once the same structure is used, there are only minor differences in the calculated eigendisplacements when using the LDA or HSE XC functional (see Fig. 8).

B. Disordered Structures

Since the presence of Cu-Zn disorder has been experimentally observed and has also been indicated as the possible reason for the discrepancies between experimental and theoretical observations [9], it is worth exploring the effect of disorder on the Raman spectra. In Fig. 6, we report the Raman spectra obtained with the LDA* approximation for the KS, CZ-PD, CZ-FD, and ST phases. The detailed analysis of the atomic decomposition of the different phonon modes (see Appendix E) reveals that the disorder does not alter the fact that the Raman active modes are associated to the motion of the S atoms, with just the addition of a minor contribution from the other elements (see Fig. 13). The disorder (be it in CZ-PD or CZ-FD) leads to the presence of several new smaller peaks in the spectrum. Their origin can most often be ascribed to the vibrations of S atoms in a specific local environment. Peaks equivalent to the A(2) and A(3) (at around 270 cm^{-1} and 320 cm^{-1} , respectively) can be identified and originate from the S atoms in a stoichiometric Cu-Cu-Zn-Sn environment, matching those obtained for KS. Most of the new peaks are instead associated with the S atoms in Cu-rich (Cu-Cu-Cu-Sn) and Cu-poor (Cu-Zn-Zn-Sn) environments. In particular, the presence of the Cu-rich S atoms leads to new phonon peaks that are more strongly shifted below 260 cm^{-1}

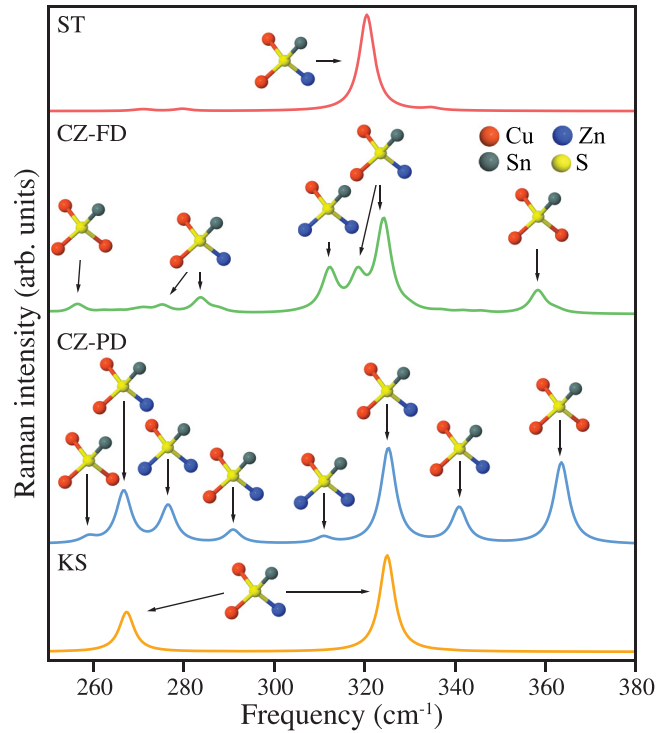


FIG. 6. Raman spectra computed using LDA* for KS, CZ-PD, CZ-FD, and ST. The local environment of the S atoms that give the largest contribution to phonon eigendisplacements is reported for each peak of the CZ-PD and CZ-FD spectra. The standard environment of KS and ST is also plotted.

and at 360 cm^{-1} . In contrast, Cu-poor S atoms induce milder shifts of the calculated peaks. It should be noted that the potential influence of the second NNs of S atoms has not been analyzed explicitly here but it most probably accounts for all the peaks that appear in the considered range.

In the calculations, the exact position of the peaks will obviously depend on the specific choice of the SQS models. Thus, in real experiments, we expect that such environments will give raise to tailing or leading edges, shouldering and splitting of the peaks. Indeed, in comparing our calculations with experiments, it should also be noted that, while in our CZ-PD and CZ-FD structures the stoichiometric, Cu-rich, and Cu-poor environments have a distribution of 50%, 25%, and 25%, respectively, the concentration of nonstoichiometric sites is expected to be much lower [5]. Therefore, we expect the actual intensities of the associated Raman peaks to be lower than in our models. This could be confirmed by performing calculations on larger SQSs, but that is still currently out of reach.

IV. CONCLUSIONS

We have analyzed the vibrational characteristics of KS, ST, and disordered CZTS phases using different XC functionals and different geometries. We have demonstrated that, since the most active modes in the Raman spectrum are entirely determined by the motion of the S atoms, the values of the associated phonon frequencies and Raman intensities are governed mainly by the value of the internal parameters u .

We have also shown that the key ingredient to tune the values of the relative intensities of the A Raman peaks are the eigendisplacements and that these depend strongly on the internal parameters u and only slightly on the XC functional employed for the calculation. In light of this, we have underlined the importance of identifying the correct internal geometry of the system to provide reliable predictions of the vibrational properties. In particular, HSE is able to reproduce the experimental lattice parameters and internal properties, as well as the phonon spectrum. Calculating the Raman spectrum from the HSE geometry leads then to an excellent overall agreement between the theoretical prediction and the experimental measurements. We have also shown that the disorder essentially accounts for the appearance of tailing or leading edges, shouldering, and splitting of the phonon peaks, and does not play a relevant role in neither their position nor their intensities.

In summary, when taking into account all the ingredients required for the calculation in the proper way, it is possible to fully explain the observed vibrational properties of the CZTS compound based mainly on the KS phase. The shape of the peaks might be exploited to qualitatively assess the disorder in the sample: the sharper the peak, the more ordered the structure.

ACKNOWLEDGMENTS

S.P.R. would like to thank the FRIA Grant of the Fonds de la Recherche Scientifique (F.R.S.-FNRS), Belgium; G.-M.R. is grateful to the Walloon Region (DGO6) through the CZTS project of the “Plan Marshall 2.vert” Program, and F.R.S.-FNRS for the financial support. Computational resources have been provided by the supercomputing facilities of the Université catholique de Louvain (CISM/UCL) and the Consortium des Equipements de Calcul Intensif en Fédération Wallonie Bruxelles (CECI) funded by the Fonds de la Recherche Scientifique de Belgique (F.R.S.-FNRS). S.P.R. would like to thank Elizabeth A. Nowadnick and Anna Miglio for insightful discussions.

APPENDIX A: SPECIAL QUASIRANDOM STRUCTURES OF DISORDERED CZTS

The special quasirandom structures (SQSs) of CZ-PD and CZ-FD were generated by MCSQS of the ATAT software suite [55]. The structures are given in Table III (CZ-PD) and Table IV (CZ-FD). The correlations of pertinent clusters are shown in Table V.

APPENDIX B: ATOMIC DECOMPOSITION OF PHONON MODES IN KS

We now analyze the atomic motion associated with the various modes and highlight the similarities and differences between the three different approximation LDA, LDA*, and HSE, for which we exploit the normalization condition of the eigendisplacements U as given in Eq. (51) of Gonze and Lee [30]:

$$\sum_{\kappa i} M_{\kappa} [U_m(\kappa i)]^* U_n(\kappa i) = \delta_{mn}, \quad (\text{B1})$$

TABLE III. Special quasirandom structure of CZ-PD (starting point). The lattice vectors (\mathbf{a}_1 , \mathbf{a}_2 , and \mathbf{a}_3) are in the unit of the lattice constant of the KS structure along \hat{x} and \hat{y} .

Lattice vectors			
	\hat{x}	\hat{y}	\hat{z}
\mathbf{a}_1	$-1/2$	$1/2$	1
\mathbf{a}_2	$-1/2$	$-1/2$	1
\mathbf{a}_3	2	0	0
Atomic coordinates			
	\mathbf{a}_1	\mathbf{a}_2	\mathbf{a}_3
Cu	$1/4$	$1/4$	$7/8$
Cu	$3/4$	$3/4$	$1/8$
Cu	0	0	0
Cu	0	0	$1/2$
Zn	$1/4$	$1/4$	$3/8$
Zu	$3/4$	$3/4$	$5/8$
Sn	$1/2$	$1/2$	$1/4$
Sn	$1/2$	$1/2$	$3/4$
S	$3/8$	$7/8$	$3/16$
S	$3/8$	$7/8$	$11/16$
S	$5/8$	$1/8$	$1/16$
S	$5/8$	$1/8$	$9/16$
S	$1/8$	$5/8$	$5/16$
S	$1/8$	$5/8$	$13/16$
S	$7/8$	$3/8$	$7/16$
S	$7/8$	$3/8$	$15/16$

where M_κ is the mass of the ion κ , i goes over the three cartesian directions, and m and n denote the phonon modes. We can identify the contribution of each atom for a given

mode as presented in Fig. 7, in which we decompose the components as parallel (\parallel) and perpendicular (\perp) to the c axis of the tetragonal cell. In this figure, they are indicated using light and dark shades of the particular color associated with each atom. Further, the $2a$, $2c$, and $2d$ sites are distinguished by forward slashes (“/”), backward slashes (“\”), and plain colors respectively.

Figure 7 shows that most of the modes have similar contributions for all the three approximations considered. In particular, all the A modes purely involve anion motion, the B modes combine cation motion \parallel to the c axis and anion motion (both \parallel and \perp), and finally the E modes involve cation motion \perp to the c axis while the anion motion is similar to the B -type modes.

One important difference concerns the fact that while under the LDA approximation the $A(1)$ and $A(2)$ modes are purely \parallel and $A(3)$ is purely \perp , the contributions are mixed for LDA* and HSE. In particular, these, that are based on the structural parameters, have a even closer set of contributions from the atomic displacements.

To analyze this aspect more clearly, similar to Eq. (B1), by using the eigendisplacements associated with two different structures, we determine an overlap between their modes by means of an overlap matrix which provides us a measure of similarity between them. The projection $p_{mn}(S_1, S_2)$ of the eigendisplacements $U_m^{S_1}$ of structure S_1 onto the eigendisplacements $U_n^{S_2}$ of structure S_2 is given by

$$p_{mn}(S_1, S_2) = \sum_{\kappa i} M_\kappa [U_m^{S_1}(\kappa i)]^* U_n^{S_2}(\kappa i). \quad (\text{B2})$$

These overlap matrices between HSE and LDA*, LDA, and HSE, and LDA and LDA* for the KS modes are shown in

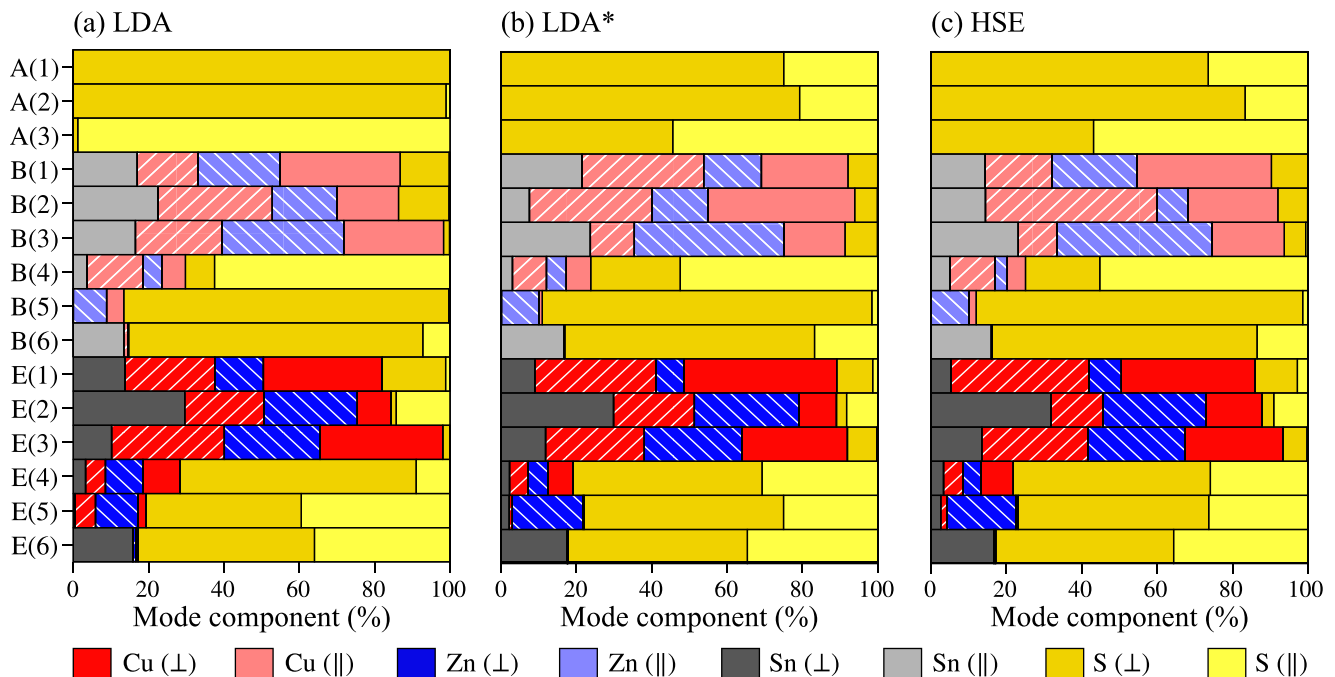


FIG. 7. Atomic decomposition of the different vibrational modes in KS as computed from (a) LDA, (b) LDA*, and (c) HSE. The contribution from the Cu, Zn, Sn, and S atoms are shown in red, blue, grey, and yellow respectively. Furthermore, for the Cu and Zn sites, the forward slashes (“/”), backward slashes (“\”) and plain colors denote the $2a$, $2c$, and $2d$ sites respectively. The parallel (\parallel) and perpendicular (\perp) components to the c axis are represented using light and dark shades of the colors associated with the different atoms.

TABLE IV. Special quasirandom structure of CZ-FD. The lattice vectors (\mathbf{a}_1 , \mathbf{a}_2 , and \mathbf{a}_3) are in the unit of the lattice constant of the KS structure along \hat{x} and \hat{y} .

Lattice vectors			
	\hat{x}	\hat{y}	\hat{z}
\mathbf{a}_1	$-1/2$	$3/2$	-1
\mathbf{a}_2	$3/2$	$-1/2$	1
\mathbf{a}_3	$1/2$	$-1/2$	-1
Atomic coordinates			
	\mathbf{a}_1	\mathbf{a}_2	\mathbf{a}_3
Cu	$2/3$	$1/3$	$2/3$
Cu	$1/3$	$2/3$	$1/3$
Cu	$1/12$	$5/12$	$5/6$
Cu	$5/12$	$1/12$	$1/6$
Cu	$7/12$	$11/12$	$5/6$
Cu	$1/4$	$1/4$	$1/2$
Zn	0	0	0
Zn	$3/4$	$3/4$	$1/2$
Zn	$11/12$	$7/12$	$1/6$
Sn	$1/6$	$5/6$	$2/3$
Sn	$1/2$	$1/2$	0
Sn	$5/6$	$1/6$	$1/3$
S	$7/8$	$5/8$	$1/2$
S	$5/24$	$7/24$	$5/6$
S	$13/24$	$23/24$	$1/6$
S	$7/24$	$17/24$	$2/3$
S	$5/8$	$3/8$	0
S	$23/24$	$1/24$	$1/3$
S	$1/8$	$7/8$	0
S	$11/24$	$13/24$	$1/3$
S	$19/24$	$5/24$	$1/6$
S	$3/8$	$1/8$	$1/2$
S	$17/24$	$19/24$	$5/6$
S	$1/24$	$11/24$	$1/6$

TABLE V. Cluster correlations (Π) for the two SQSs. The clusters are sorted by diameter (d). The point functions are $+1$ and -1 for Cu and Zn sites, respectively. The correlations for the ideally random structure are shown for reference.

Pairs	d (a_{lat})	CZ-PD		CZ-FD	
		Π_{SQS}	Π_{ideal}	Π_{SQS}	Π_{ideal}
Pairs	$\sqrt{1/2}$	0	0	0	1/9
	1	0	0	1/6	1/9
		0	0	1/3	1/9
	$\sqrt{3/2}$	0	0	$-1/3$	1/9
		0	0	$-1/3$	1/9
	Triplets	$\sqrt{2}$	0	0	$-1/6$
$\sqrt{2}$		-1	0	0	1/9
		1	0	0	1/9
$\sqrt{2}$		-1	0	1/3	1/9
		0	0	1/3	1/9
$\sqrt{5/2}$		0	0	0	1/9
	0	0	1/3	1/9	
Triplets	$\sqrt{3}$	0	0	0	1/9
	$\sqrt{1/2}$	0	0	1/6	1/9
		0	0	$-1/3$	1/27
	1	0	0	1/3	1/27
		0	0	0	1/27
	0	0	0	1/3	1/27
0	0	0	0	1/27	

Figs. 8, 9, 10. The overlap matrix between HSE and LDA* shows that they are very similar except for the slight mixing in two B and two E modes. In particular, the overlap of the A modes is very high, confirming that the phonon modes with the highest Raman activity are already well captured by the LDA* calculation. On the other hand, we find large dissimilarities in the A modes when comparing the LDA with the other two approximations. This can be once again ascribed to the change in the value of the internal parameters u .

APPENDIX C: u_y AND u_z DEPENDENCE

Figures 11 and 12 represent the dependency of the A modes phonon frequencies and Raman intensities as function of u_y and u_z , respectively.

APPENDIX D: BOND POLARIZABILITY MODEL FOR THE A MODES

The Raman susceptibility tensor α_m , which appears in Eq. (1) is given by

$$\alpha_{ij}^m = \sqrt{\Omega} \sum_{\kappa k} \frac{\partial \chi_{ij}}{\partial \tau_{\kappa k}} U_m(\kappa k) \quad (\text{D1})$$

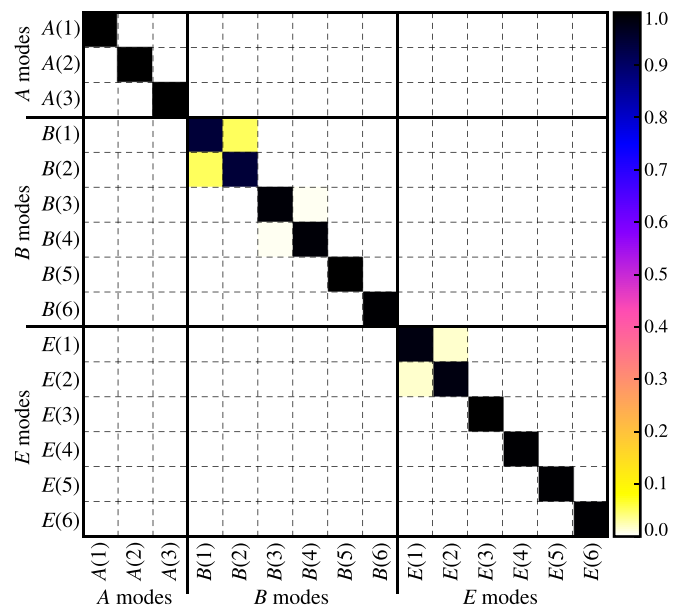


FIG. 8. Overlap matrix between KS modes computed with HSE and LDA*.

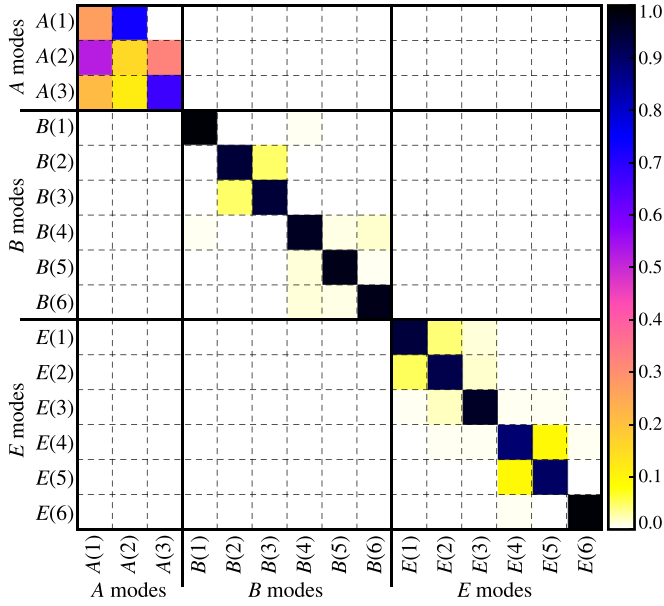


FIG. 9. Overlap matrix between KS modes computed with LDA and HSE.

where Ω is the volume of the cell, $\tau_{\kappa k}$ are the three cartesian coordinates of atom κ , and χ_{ij} is the electric polarizability tensor:

$$\chi_{ij} = \frac{\epsilon_{ij}^{\infty} - \delta_{ij}}{4\pi}. \quad (\text{D2})$$

In the bond polarizability model (BPM) [54,56], it is obtained as the sum of bond contributions:

$$\chi_{ij} = \sum_{\kappa\kappa'} \tilde{\chi}_{ij}(\kappa\kappa'). \quad (\text{D3})$$

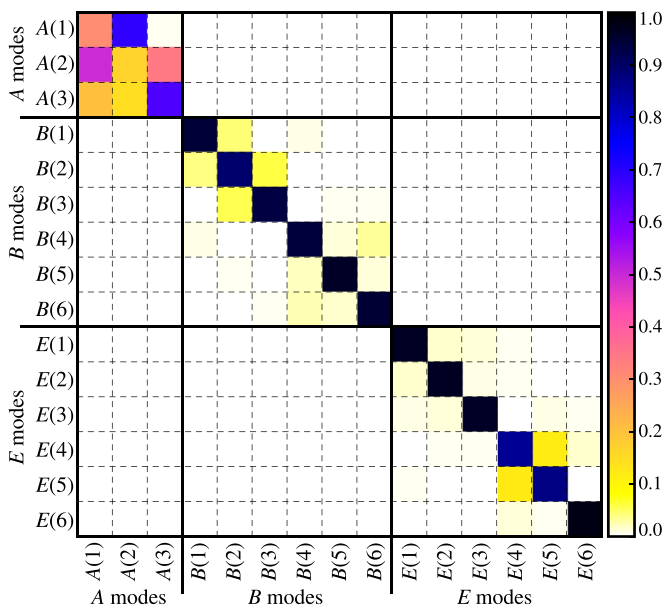


FIG. 10. Overlap matrix between KS modes computed with LDA and LDA*.

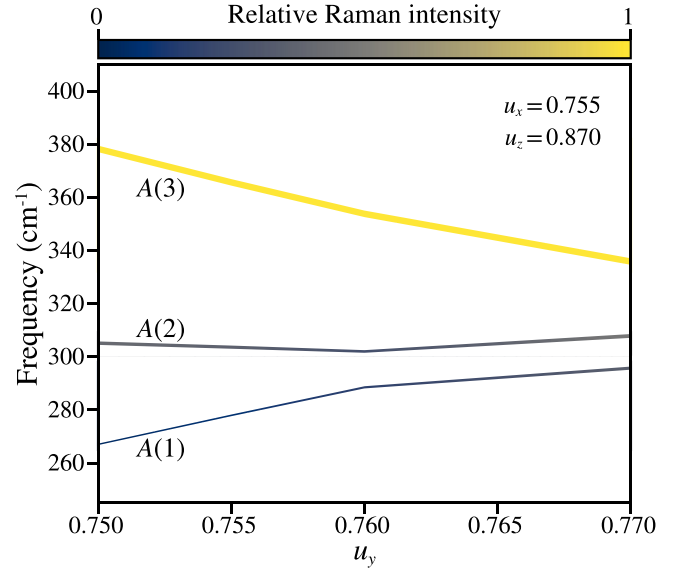


FIG. 11. Variation of the frequencies for the A phonon modes of KS structure calculated within the LDA approximation as a function of the u_y parameter. The evolution of the corresponding relative Raman intensities is indicated by the color and thickness of the lines. u_x and u_z are kept fixed.

And, omitting $(\kappa\kappa')$ in order to simplify the notation, these bond contributions are expressed as

$$\tilde{\chi}_{ij} = \frac{2\beta_p + \beta_l}{3} \delta_{ij} + (\beta_l - \beta_p) \left(\frac{R_i R_j}{R^2} - \frac{1}{3} \delta_{ij} \right) \quad (\text{D4})$$

where $\mathbf{R} = \tau_{\kappa} - \tau_{\kappa'}$ is a vector, which defines the direction and the distance of a pair of nearest-neighbor atoms at sites κ

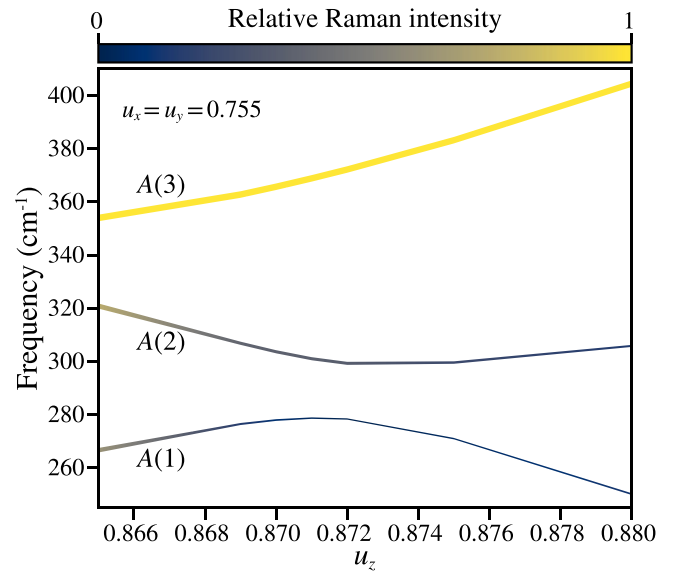


FIG. 12. Variation of the frequencies for the A phonon modes of KS structure calculated within the LDA approximation as a function of the u_z parameter. The evolution of the corresponding relative Raman intensities is indicated by the color and thickness of the lines. $u_x = u_y$ are kept fixed.

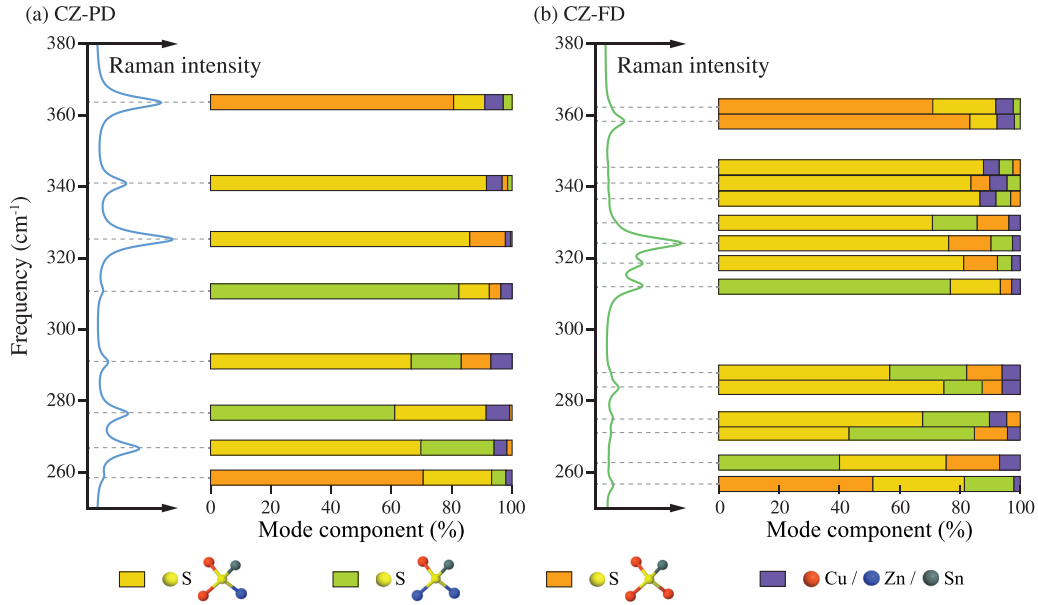


FIG. 13. Atomic decomposition of the active Raman modes for (a) CZ-PD and (b) CZ-FD in the LDA* approximation. The contribution originating from the S atoms is further split according to their local environment: stoichiometric (Cu-Cu-Zn-Sn) in yellow, Cu-rich (Cu-Cu-Cu-Sn) in orange, and Cu-poor (Cu-Zn-Zn-Sn) in green, respectively. Contributions from Cu, Zn, and Sn are grouped and depicted in purple. For each peak, the different atomic contributions are sorted in decreasing order from left to right.

and κ' . The parameters β_l and β_p correspond to the longitudinal and perpendicular bond polarizability, respectively.

The BPM further assumes that β_l and β_p only depend on the length of the bond. Therefore, the derivative of the bond contributions $\tilde{\chi}_{ij}$ with respect to the displacement of the atom κ in the direction k is given by

$$\frac{\partial \tilde{\chi}_{ij}}{\partial \tau_{\kappa k}} = \gamma_1 \delta_{ij} \hat{R}_k + \gamma_2 \left(\hat{R}_i \hat{R}_j - \frac{1}{3} \delta_{ij} \right) \hat{R}_k + \gamma_3 (\delta_{ik} \hat{R}_j + \delta_{jk} \hat{R}_i - 2 \hat{R}_i \hat{R}_j \hat{R}_k) \quad (\text{D5})$$

where $\hat{\mathbf{R}}$ is a unit vector along \mathbf{R} and the three parameters γ_1 , γ_2 , and γ_3 are defined as

$$\gamma_1 = \frac{2\beta'_p + \beta'_l}{3}, \quad \gamma_2 = \beta'_l - \beta'_p, \quad \gamma_3 = \frac{\beta_l - \beta_p}{R} \quad (\text{D6})$$

where β'_l and β'_p are the derivatives of the longitudinal and perpendicular bond polarizabilities with respect to the bond length. Each different kind of bond is characterized by three such values.

For the A and \tilde{A} modes, the Raman susceptibility tensors take the following form:

$$\begin{pmatrix} a & & \\ & a & \\ & & b \end{pmatrix}. \quad (\text{D7})$$

Since only S atoms move in these modes, the only nonzero terms of the sum in Eq. (D1) are those for which κ is one of these atoms [$U_m(\kappa k) = 0$ if κ is not one of them]. Hence, in the BPM, the only important contributions are originating from the bonds involving S atoms. In our structures, there are four types of such bonds: those connecting the S atoms with the atoms sitting on the $2a$, $2b$, $2c$, and $2d$ sites. We will thus label the corresponding parameters of the model

with a superscript referring to the Wyckoff site. With this information, it can be shown that

$$a(\tilde{A}') = K(\Delta_1^{cd} + \Delta_3^{cd})a(\tilde{A}'') = K(\Delta_1^{ab} + \Delta_3^{ab}) \quad (\text{D8})$$

$$a(\tilde{A}''') = K\sqrt{2}((\Sigma_1^{ab} - \Sigma_1^{cd}) + 2(\Sigma_3^{ab} - \Sigma_3^{cd}))$$

$$b(\tilde{A}') = K(\Delta_1^{cd} - 2\Delta_3^{cd})b(\tilde{A}'') = K(\Delta_1^{ab} - 2\Delta_3^{ab})$$

$$b(\tilde{A}''') = K\sqrt{2}((\Sigma_1^{ab} - \Sigma_1^{cd}) - 4(\Sigma_3^{ab} - \Sigma_3^{cd})) \quad (\text{D9})$$

with $K = \sqrt{\frac{32}{27M_S}}$ where M_S is the atomic mass of S, $\Delta_i^{xy} = \gamma_i^{2x} - \gamma_i^{2y}$ and $\Sigma_i^{xy} = \gamma_i^{2x} + \gamma_i^{2y}$ for $i=1, 2, 3$ and $x, y = a, b, c$.

We note that, for the structures considered in this study, $\gamma_2 = \beta'_l - \beta'_p$ does not contribute to any of the Raman intensities. Furthermore, all the polarizability parameters (β_l , β_p , β'_l , and β'_p) appear at the second order (either squared or as a mixed product).

Within such a BPM, the rigid rotation of a tetrahedron does not contribute at all to the Raman intensity. As a result, the tetrahedra with the Sn atom and the atom sitting on the $2a$ site (in grey and blue, respectively) at their center do not contribute to the intensity of the \tilde{A}' mode, which is thus simply related to the difference in the polarizability parameters of the bonds involving the atoms sitting on the $2c$ and $2d$ sites (in green and red, respectively) because the S atoms surrounding them move in opposite directions. In ST, the occupations of those two sites are exactly the same on average (and so do the corresponding bond polarizability parameters) and thus the \tilde{A} mode becomes silent. Similarly, the tetrahedra with the atoms sitting on the $2c$ and $2d$ sites at their center do not contribute to the intensity of the \tilde{A}'' mode, which depends solely on the difference in the polarizability parameters of the bonds involving the Sn atom and the atom sitting on the

2a site. Finally, the intensity of the \tilde{A}''' mode will depend on the difference between, on the one hand, the sum of the polarizability parameters of the bonds involving the Sn atom and the atom sitting on the 2a site, and, on the other hand, the sum of the polarizability parameters of the bonds involving the atoms sitting on the 2c and 2d sites.

APPENDIX E: ATOMIC DECOMPOSITION OF PHONON MODES IN DISORDERED STRUCTURES

In Fig. 13, we report the atomic decomposition introduced in Eq. (B1) for the Raman active modes in the frequency range between 250 and 380 cm^{-1} . In particular, we distinguish the contribution of the S atoms with different local environments: stoichiometric (Cu-Cu-Zn-Sn) in yellow, Cu-

rich (Cu-Cu-Cu-Sn) in orange, and Cu-poor (Cu-Zn-Zn-Sn) in green. At variance with the ordered structures, a small contribution originating from the Cu, Zn, and Sn vibrations can be observed for all the modes, though it remains negligible. The figure shows that, for most of the modes, it is possible to identify a type of S atom whose contribution is prevalent with respect to the others.

Large contributions from stoichiometric S can be found in the region of the original KS peaks (270 cm^{-1} and 320 cm^{-1}). Modes with prevalent contributions from the Cu-rich environments appear near the edges of the considered region of the spectrum (260 cm^{-1} and 360 cm^{-1}). Cu-poor environments lead to smaller shifts, with modes still localized in the vicinity of the original peaks.

-
- [1] C. Breyer, D. Bogdanov, A. Gulagi, A. Aghahosseini, L. S. Barbosa, O. Koskinen, M. Barasa, U. Caldera, S. Afanasyeva, M. Child *et al.*, *Prog. Photovoltaics Res. Appl.* **25**, 727 (2017).
- [2] M. A. Green, Y. Hishikawa, W. Warta, E. D. Dunlop, D. H. Levi, J. Hohl-Ebinger, and A. W. Ho-Baillie, *Prog. Photovoltaics Res. Appl.* **25**, 668 (2017).
- [3] C. Yan, J. Huang, K. Sun, S. Johnston, Y. Zhang, H. Sun, A. Pu, M. He, F. Liu, K. Eder *et al.*, *Nat. Energy* **3**, 764 (2018).
- [4] S. Bourdais, C. Choné, B. Delatouche, A. Jacob, G. Larramona, C. Moisan, A. Lafond, F. Donatini, G. Rey, S. Siebentritt *et al.*, *Adv. Energy Mater.* **6**, 1502276 (2016).
- [5] W. Chen, D. Dahliah, G.-M. Rignanese, and G. Hautier, *Energy Environ. Sci.* **14**, 3567 (2021).
- [6] S. Schorr, *Sol. Energy Mater. Sol. Cells* **95**, 1482 (2011).
- [7] J. J. Scragg, L. Choubrac, A. Lafond, T. Ericson, and C. Platzer-Björkman, *Appl. Phys. Lett.* **104**, 041911 (2014).
- [8] J. M. Skelton, A. J. Jackson, M. Dimitrievska, S. K. Wallace, and A. Walsh, *APL Mater.* **3**, 041102 (2015).
- [9] S. P. Ramkumar, Y. Gillet, A. Miglio, M. J. van Setten, X. Gonze, and G.-M. Rignanese, *Phys. Rev. B* **94**, 224302 (2016).
- [10] M. Dimitrievska, F. Boero, A. P. Litvinchuk, S. Delsante, G. Borzone, A. Perez-Rodríguez, and V. Izquierdo-Roca, *Inorg. Chem.* **56**, 3467 (2017).
- [11] M. Paris, G. Larramona, P. Bais, S. Bourdais, A. Lafond, C. Choné, C. Guillot-Deudon, B. Delatouche, C. Moisan, and G. Denmler, *J. Phys. Chem. C* **119**, 26849 (2015).
- [12] M. Paris, L. Choubrac, A. Lafond, C. Guillot-Deudon, and S. Jobic, *Inorg. Chem.* **53**, 8646 (2014).
- [13] J. J. Scragg, J. K. Larsen, M. Kumar, C. Persson, J. Sendler, S. Siebentritt, and C. Platzer Björkman, *Phys. Status Solidi B* **253**, 247 (2016).
- [14] S. Schorr, H.-J. Hoebler, and M. Tovar, *Eur. J. Mineral.* **19**, 65 (2007).
- [15] A. Lafond, L. Choubrac, C. Guillot-Deudon, P. Fertey, M. Evain, and S. Jobic, *Acta Crystallogr. B* **70**, 390 (2014).
- [16] A. Ritscher, M. Hoelzel, and M. Lerch, *J. Solid State Chem.* **238**, 68 (2016).
- [17] C. J. Bosson, M. T. Birch, D. P. Halliday, K. S. Knight, A. S. Gibbs, and P. D. Hatton, *J. Mater. Chem. A* **5**, 16672 (2017).
- [18] S. P. Ramkumar, A. Miglio, M. J. van Setten, D. Waroquiers, G. Hautier, and G.-M. Rignanese, *Phys. Rev. Materials* **2**, 085403 (2018).
- [19] S. K. Wallace, J. M. Frost, and A. Walsh, *J. Mater. Chem. A* **7**, 312 (2019).
- [20] Y.-F. Zheng, J.-H. Yang, and X.-G. Gong, *AIP Adv.* **9**, 035248 (2019).
- [21] M. Dimitrievska, A. Fairbrother, X. Fontané, T. Jawhari, V. Izquierdo-Roca, E. Saucedo, and A. Pérez-Rodríguez, *Appl. Phys. Lett.* **104**, 021901 (2014).
- [22] X. Fontané, V. Izquierdo-Roca, E. Saucedo, S. Schorr, V. Yuhymchuk, M. Y. Valakh, A. Pérez-Rodríguez, and J. Morante, *J. Alloys Compd.* **539**, 190 (2012).
- [23] A.-J. Cheng, M. Manno, A. Khare, C. Leighton, S. A. Campbell, and E. S. Aydil, *J. Vac. Sci. Tech. A* **29**, 051203 (2011).
- [24] A. Khare, B. Himmetoglu, M. Johnson, D. J. Norris, M. Cococcioni, and E. S. Aydil, *J. Appl. Phys.* **111**, 083707 (2012).
- [25] M. Guc, S. Levchenko, I. V. Bodnar, V. Izquierdo-Roca, X. Fontane, L. V. Volkova, E. Arushanov, and A. Pérez-Rodríguez, *Sci. Rep.* **6**, 19414 (2016).
- [26] T. Gürel, C. Sevik, and T. Çağın, *Phys. Rev. B* **84**, 205201 (2011).
- [27] B. Monserrat, J.-S. Park, S. Kim, and A. Walsh, *Appl. Phys. Lett.* **112**, 193903 (2018).
- [28] P. Hohenberg and W. Kohn, *Phys. Rev.* **136**, B864 (1964).
- [29] P. Giannozzi, S. de Gironcoli, P. Pavone, and S. Baroni, *Phys. Rev. B* **43**, 7231 (1991).
- [30] X. Gonze and C. Lee, *Phys. Rev. B* **55**, 10355 (1997).
- [31] X. Gonze, *Phys. Rev. B* **55**, 10337 (1997).
- [32] X. Gonze, J.-M. Beuken, R. Caracas, F. Detraux, M. Fuchs, G.-M. Rignanese, L. Sindic, M. Verstraete, G. Zerah, F. Jollet *et al.*, *Comput. Mater. Sci.* **25**, 478 (2002).
- [33] X. Gonze, B. Amadon, P.-M. Anglade, J.-M. Beuken, F. Bottin, P. Boulanger, F. Bruneval, D. Caliste, R. Caracas, M. Côté *et al.*, *Comput. Phys. Commun.* **180**, 2582 (2009).
- [34] X. Gonze, F. Jollet, F. A. Araujo, D. Adams, B. Amadon, T. Applencourt, C. Audouze, J.-M. Beuken, J. Bieder, A. Bokhanchuk *et al.*, *Comput. Phys. Commun.* **205**, 106 (2016).
- [35] D. R. Hamann, *Phys. Rev. B* **88**, 085117 (2013).

- [36] K. Lejaeghere, G. Bihlmayer, T. Björkman, P. Blaha, S. Blügel, V. Blum, D. Caliste, I. E. Castelli, S. J. Clark, A. Dal Corso *et al.*, *Science* **351**, aad3000 (2016).
- [37] M. Van Setten, M. Giantomassi, E. Bousquet, M. J. Verstraete, D. R. Hamann, X. Gonze, and G.-M. Rignanese, *Comput. Phys. Commun.* **226**, 39 (2018).
- [38] W. Kohn and L. J. Sham, *Phys. Rev.* **140**, A1133 (1965).
- [39] H. J. Monkhorst and J. D. Pack, *Phys. Rev. B* **13**, 5188 (1976).
- [40] M. Veithen, X. Gonze, and P. Ghosez, *Phys. Rev. B* **71**, 125107 (2005).
- [41] Y. Gillet, M. Giantomassi, and X. Gonze, *Phys. Rev. B* **88**, 094305 (2013).
- [42] R. Caracas and E. J. Banigan, *Phys. Earth Planet. Inter.* **174**, 113 (2009).
- [43] J. Heyd, G. E. Scuseria, and M. Ernzerhof, *J. Chem. Phys.* **118**, 8207 (2003).
- [44] A. V. Krugau, O. A. Vydrov, A. F. Izmaylov, and G. E. Scuseria, *J. Chem. Phys.* **125**, 224106 (2006).
- [45] M. C. Payne, M. P. Teter, D. C. Allan, T. Arias, and J. Joannopoulos, *Rev. Mod. Phys.* **64**, 1045 (1992).
- [46] G. Kresse and J. Furthmüller, *Comp. Mater. Sci.* **6**, 15 (1996).
- [47] P. E. Blöchl, *Phys. Rev. B* **50**, 17953 (1994).
- [48] A. Togo and I. Tanaka, *Scr. Mater.* **108**, 1 (2015).
- [49] A. Zunger, S.-H. Wei, L. G. Ferreira, and J. E. Bernard, *Phys. Rev. Lett.* **65**, 353 (1990).
- [50] S. Botti, D. Kammerlander, and M. A. L. Marques, *Appl. Phys. Lett.* **98**, 241915 (2011).
- [51] J. Vidal, S. Botti, P. Olsson, J.-F. Guillemoles, and L. Reining, *Phys. Rev. Lett.* **104**, 056401 (2010).
- [52] S. M. Hall, J. T. Szymanski, and J. M. Stewart, *Canad. Mineral.* **16**, 131 (1978).
- [53] M. Himmrich and H. Haeuselner, *Spectrochim. Acta A* **47**, 933 (1991).
- [54] P. Umari, A. Pasquarello, and A. Dal Corso, *Phys. Rev. B* **63**, 094305 (2001).
- [55] A. van de Walle, P. Tiwary, M. de Jong, D. Olmsted, M. Asta, A. Dick, D. Shin, Y. Wang, L.-Q. Chen, and Z.-K. Liu, *Calphad* **42**, 13 (2013).
- [56] R. Tubino and L. Piseri, *Phys. Rev. B* **11**, 5145 (1975).